Mapping Structural Aging across Human Tissues reveals tissue-specific trajectories, coordinated deterioration and genetic determinants

Anamika Yadav[1], Kyle Alvarez[1], Kevin Yip[1], Veronica Gomez-Lobo[2], Eytan Ruppin[3], Caroline Kumsta[4], Sanju Sinha[1,†]
1. Center of Data Science, Sanford Burnham Prebys Medical Discovery Institute, La Jolla, CA, USA.
2. Eunice Kennedy Shriver National Institute of Child Health and Human Development, National Institutes of Health, Bethesda, Maryland, USA.
3. Cancer Data Science Lab, National Cancer Institute, National Institutes of Health, Bethesda, Maryland, USA.
4. Center for Cardiovascular and Muscular Diseases, Sanford Burnham Prebys Medical Discovery Institute, La Jolla, CA, USA.
† Corresponding author

1. Abstract

Tissue structure, the organization of cells, vasculature and extracellular matrix, determines organ function. Yet how tissue structure changes with aging remains largely unknown. Current aging research primarily focuses on molecular changes, missing this structural dimension. Here, we present **P**ath**S**t**AR**, **P**athology based **S**tructural **A**ging **R**ate, the first computational framework that captures when and how tissue structure changes during aging from histopathology images. We applied it to 25,306 postmortem tissues covering 40 tissue types from individuals aged 21–70, connecting structural aging to molecular data, health records and genotype data. Without any training on chronological age, PathStAR captured non-linear functional decline of ovary, undetectable by bulk-molecular profiling. Applying it across 40 tissues, it revealed that structural aging occurs through discrete phases of rapid change (accelerated periods), with tissue-specific trajectories following three patterns: *Early Aging Tissues* (vascular system with major changes during the 30s), *Late Aging Tissues* (uterus and vagina with major changes during menopause (50s)) and *Biphasic Aging Tissues* (digestive, male reproductive tissues, and ovary with two periods of major changes). During these accelerated phases, most tissues exhibited shared aging hallmarks of inflammation and energy production decline, coupled with disruption of pathways governing their specialized functions. Cross-organ analysis revealed coordinated aging within organ systems and an unexpected link between digestive and male reproductive tissues. We next identified 123 germline variants associated with organ-specific accelerated structural aging, including SIRT6 variants linked to accelerated vascular decline. Finally, individuals with systemic autoimmune disease, as well as tissues with classical aging pathologies (atrophy, calcification, fibrosis), showed elevated structural aging scores.

We demonstrate that structural aging is measurable from histology scans and provide the first systematic framework for studying it, revealing organ-specific aging processes.

2. Introduction

Aging is the biggest risk factor for most chronic diseases, including cardiovascular disease, Type 2 diabetes, Alzheimer's disease, and many cancers [1]. Current aging research has advanced our understanding of molecular changes during aging, both cell intrinsic like telomeres shortening, cell senescence, and autophagy, as well as systemic pathways like the insulin/IGF-1 axis [1, 2, 3, 4]. Aging clocks, either from methylation or other omics layers, can enabled improved prediction of risk of mortality and diseases [5, 6]. Complementing these clocks, recent studies showed that molecular changes during aging unfolds through discrete, non-linear transitions rather than gradual decline, in blood multi-omics [7] as well as in tissues proteomics [8].

While we have advanced our knowledge of molecular, cellular and systemic changes during aging, a critical missing gap remains in understanding how the physical structure of tissues, the spatial organization of cells, vasculature and extracellular matrix, and the basis of their function, deteriorates with aging (*Structural Aging*). Our current understanding of tissue structural aging comes from manual inspection of histology images revealing both global deterioration patterns like fiber fragmentation [9,10], atrophy [11], and fibrosis [12], and, tissue-specific patterns like ovarian follicle loss [13], bone porosity [14], brain cortical thinning and demyelination, muscle atrophy [15], arterial stiffening [16], heart fibrosis [17,18] , thymic involution [19], and lens clouding [20]. These structural changes precede both decline of organ function with age and diseases, e.g. ovarian follicle loss reducing fertility and cardiac fibrosis increasing heart failure risk. However, despite these specific examples, currently there is no systematic study to capture generalizable tissue structure changes during aging. This gap has persisted due to lack of large-scale high-resolution tissue images across the body and computational tools to quantify these tissue sub-structures.

These limitations have given rise to several fundamental open questions about aging: When and how do different tissue physical structures deteriorate during aging? What are their molecular drivers? Are there tissue-specific periods of accelerated structural aging, and what molecular dysregulation drives this acceleration? Which organs are early-agers versus late-agers? Is there cross-organ coordination in structural aging, and what signaling molecules drive this coordination? How do lifestyle and clinical factors accelerate or protect against structural aging? And finally, how do germline variants affect organ-specific structural aging trajectories?

We developed a computational method to quantify structural aging of tissues from histopathology slides, PathStAR (Pathology-based Structural Aging) and present the first systematic study to tackle these questions at scale. We applied PathStAR to 25,306 post-mortem biopsies across 40 tissue types from 970 individuals (ages 21–70) in the Genotype-Tissue Expression (GTEx) cohort [21], originally designed to understand expression regulatory network and is the largest public repository of non-diseased human tissues with matched transcriptomic, methylation, clinical, and germline data.

As proof-of-concept, PathStAR successfully captures, *without training on chronological age*, an established non-linear ovarian functional decline—fertility decline in the 30s and menopause in the 50s, that transcriptomics or methylation profiles from identical samples failed to detect. We applied it across 40 tissues, identifying tissue-specific structural aging trajectories and periods of accelerated changes. During these accelerated phases, most tissues showed increased inflammation, decreased energy generation, and reduced cell division capacity, alongside tissue-specific disruptions like impaired arterial lipid processing and diminished estrogen response in female reproductive organs. PathStAR next revealed coordinated deterioration among tissues within an organ system and unexpected correlation among digestive and reproductive structural aging. Connecting individual-tissue structural aging scores to clinical and genotype data revealed protective and detrimental variants of organ-specific aging, and effect of different diseases on tissues-specific structural aging. Overall, our framework complements molecular-based analyses of aging, to establish how and when different tissue structures age and then study their molecular underpinnings in a morphologically guided manner.

3. Result

3.1 Overview of PathStAR Pipeline

Tissue structure is critical for its function and thus learning how and when it changes during aging is crucial. Based on the notion that histopathology images capture architecture features critical for tissue function, we developed a computational framework called ***PathStAR*** (Figure 1A-C), that quantify how and when this tissue structure changes during aging from high-resolution H&E images of large-scale post-mortem biopsies. PathStAR was applied on (GTEx cohort) post-mortem biopsies from 970 non-diseased individuals (age range = 21-70 years, 66.4% males, **Figure S1**) spanning 40 tissue types (**Figure 1D**). This provided a total of 25,306 biopsy whole-slide scans (×20 magnification), 30.3 million patch images (512 × 512 pixels). Pathology annotations from GTEx for these images confirmed canonical aging-related increase in atrophy, fibrosis, cysts, atherosclerosis, and decrease in ovum, spermatogenesis, and of protective layers including mucosa, endo- and myometrium

(**Figure S2**), demonstrating quality to develop a systematic method. Tissue-specific quality control analysis is presented in **Notes S1**.

PathStAR has three steps (**Figure 1A-C** & detailed below). **(1)** First, we extract morphological features from histopathology slides using a pre-trained vision transformer, converting visual structural patterns into quantitative data. **(2)** Second, we quantify the rate of structural changes per year, which we term Structural Aging Rate. We compute this rate across ages 21-70 to generate aging trajectories and identify periods of substantial change. **(3)** Third, we calculate individual delta-structural aging scores that measure each sample's deviation from the expected population trajectory in (2), As downstream analyses, we integrate the structural aging trajectory and individual-level scores with transcriptomics, methylation, health records, lifestyle factors, and germline variants to identify molecular correlates and determinants of structural aging patterns. We control for both post-mortem and technical artifacts via a multi-variate regression and report their contribution in PathStAR's outputs variance. We describe PathStAR's three steps in detail below:

I. *Feature Extraction from Whole Slide Images (WSI):* For a given H&E image, we start by leveraging the UNI vision encoder [22](**Figure 1A**, *top panel*), a large vision transformer (ViT) pre-trained on the 100K whole-slide images (Mass-100K dataset) using DINOv2 self-supervised learning. UNI was chosen over other foundation models primarily due to diverse training data including non-cancer slides (details in Notes S2). After background removal, each WSI is segmented into patches that are processed through UNI to extract 1024-dimensional feature embeddings (detailed in methods section 5.3). These patch-level features are aggregated using mean pooling (average across all patched) to create whole-slide representations. A UMAP based on these whole-slide representations segregate different tissues (**Figure 1E**) suggesting that these features capture tissue-specific morphological features. They can further segregate tissue substructures as illustrated in **Figure 1F**.

II. *Structural Aging Rate and Trajectory:* We next asked: when does tissue structure change most rapidly during aging? Since we have limited samples per individual year, we used sliding 10-year windows to compare tissue structure between consecutive age groups. This measures how much tissue structure changes per year, which we term Structural Aging Rate. We computed this rate across ages 30-79 for tissues with sufficient samples (≥200), stratifying by sex (details in **Methods 5.3**). This revealed tissue-specific trajectories showing when structural aging accelerates or slows down during the human lifespan. We identified periods where structural aging rate peaks and termed these *Accelerated Structural Aging (**ASA**) periods* – age periods when tissue structure undergoes rapid transformation.

III. *Individual Tissue-Specific Scores:* Using population-level structural aging trajectories from Step 2, we compute individual delta-structural aging scores that quantify

deviation from expected aging trajectory (**Figure 1C**). For each sample, we calculate the effect size difference between the individual's morphological features and a 10-year younger reference window from the same tissue type details in **Methods 5.3**. These delta-structural-aging scores enable direct comparison across individuals and identification of samples with atypical aging patterns, facilitating downstream analysis of factors that accelerate or protect against tissue structural deterioration.

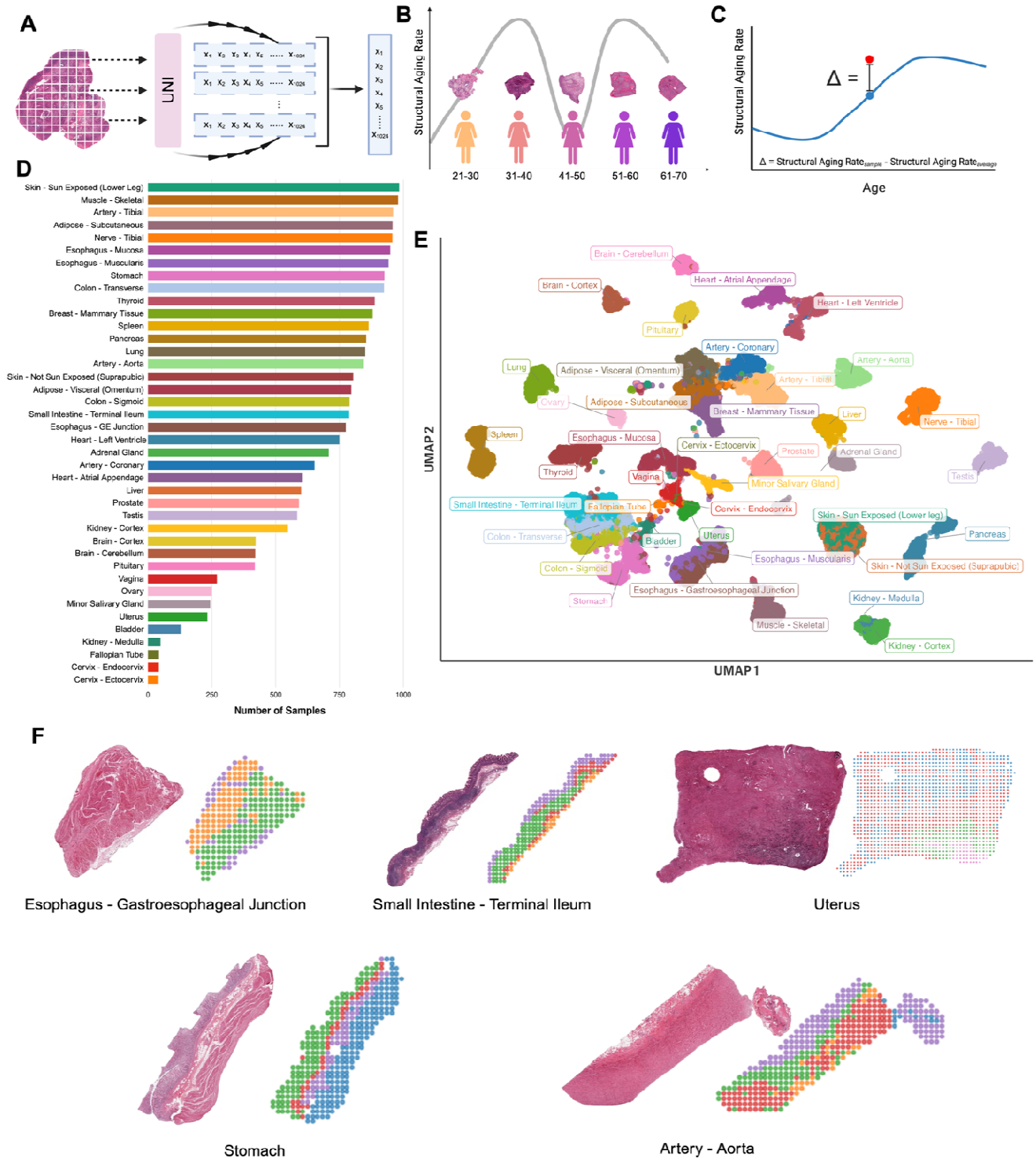

Fig 1: Overview of PathStAR pipeline Steps and GTEx cohort used here: **(A-C)** *PathStAR starts (Step 1: Feature extraction) by extracting morphology feature of 256*256 pixels patch-level using a pre-trained pathology foundation model (UNI) which are aggregated (mean pooling) to generate slide-level representation. It then computes structural aging rate by quantifying the rate of morphological change per year using sliding 10-year windows, generating age-specific trajectories that reveal periods of Accelerated*

Structural Aging periods. Finally, it computes individual delta-structural aging scores (red) measuring each sample's deviation from the population aging trajectory (blue). **(D)** *Number of samples available for this study per tissue type.* **(E)** *UMAP based on whole-slide level representation cluster different tissue types, demonstrating its ability to capture tissue type-specific morphological properties.* **(F)** *Morphological patch level features from UNI clustered using spatial information and K-means, where different colors are different clusters.*

3.2 PathStAR captures ovary's functional decline and its molecular correlates without chronological age training

3.2.1 Morphology Captures Ovary's Non-Linear Functional Decline

Aging may occur gradually or in distinct phases. Ovary exhibits a non-linear trajectory of reproductive decline: fertility decreases gradually from the early 30s, marked by rapid follicular depletion that accelerates through the late 30s, and culminates in menopause at approximately 50–55 years of age [23, 24]. Notably, current molecular clocks, either based on expression or methylation, are trained on chronological age, assume linear aging and thus cannot capture this non-linear ovary remodeling (**Figure S3)**. To test whether PathStAR could overcome this limitation, we first validated it on ovarian tissue, asking if morphology alone, without any training on chronological age, could reveal these well-established transitions.

We first found that the UNI-based morphological features can segregate distinct ovary substructures (**Figure 2A-B, Figure S4**). We also found that the ovary's morphology features can segregate young, middle age vs. old ovaries suggesting substantial change during aging (**Figure 2C,** *PC 1-2 correlation with age***,** $r^2 = 0.43$). This suggests that ovary structure substantially changes during aging that morphology can segregate young vs. old ovary, *without training on chronological age*. Building on this, we next applied PathStAR to compute the structural aging trajectory across 250 ovary biopsies (age range: 21-79 years), quantifying the rate of structural aging (**Figure 2F**). This yielded a striking bimodal pattern with two peaks of accelerated structural aging aligning with established reproductive milestones (**Figure 2F**, Methods 5.3). The first **A**ccelerated **S**tructural **A**ging (ASA) period peaks at ages 35-40, coinciding with fertility decline, while the second ASA period peaks at ages 55-60, corresponding to menopause. Importantly, ischemic time and other post-mortem artifacts showed minimal correlation with this trajectory (**Notes S3, Figure S5**).

3.2.2 Molecular Approaches Fail to Detect Ovary's Non-Linear Decline

We next asked <u>whether applying the same trajectory analysis to molecular data from the same tissue samples would capture this functional decline milestone</u> (**Methods 5.4).** Using expression or methylation profile from same samples, we found that while expression can segregate young vs. old samples (albeit with lower power than H&E, r^2=0.3, **Figure 2D**), neither expression nor methylation profile capture this bimodal

remodeling trajectory and functional decline of ovary (**Figure 2 G, H**). Beyond total structural-aging rate, specific structural feature groups, commonly increasing, or decreasing or not changing were also identified and described in **Notes S4** (**Figure 2I,J, S6, Method 5.5)**.

To interpret the structural changes during the two ASA periods, we used a vision-language model (PLIP [25]). We first validated that PLIP against pathologist annotations, confirming its ability to capture ovary-specific morphology (**Notes S3, Figure S7**). Applying PLIP to biopsies from each ASA period revealed an increase in fibrosis and atrophy during both ASA periods along with a pronounced decline in ovum abundance during second ASA period **(Figure S8)**.

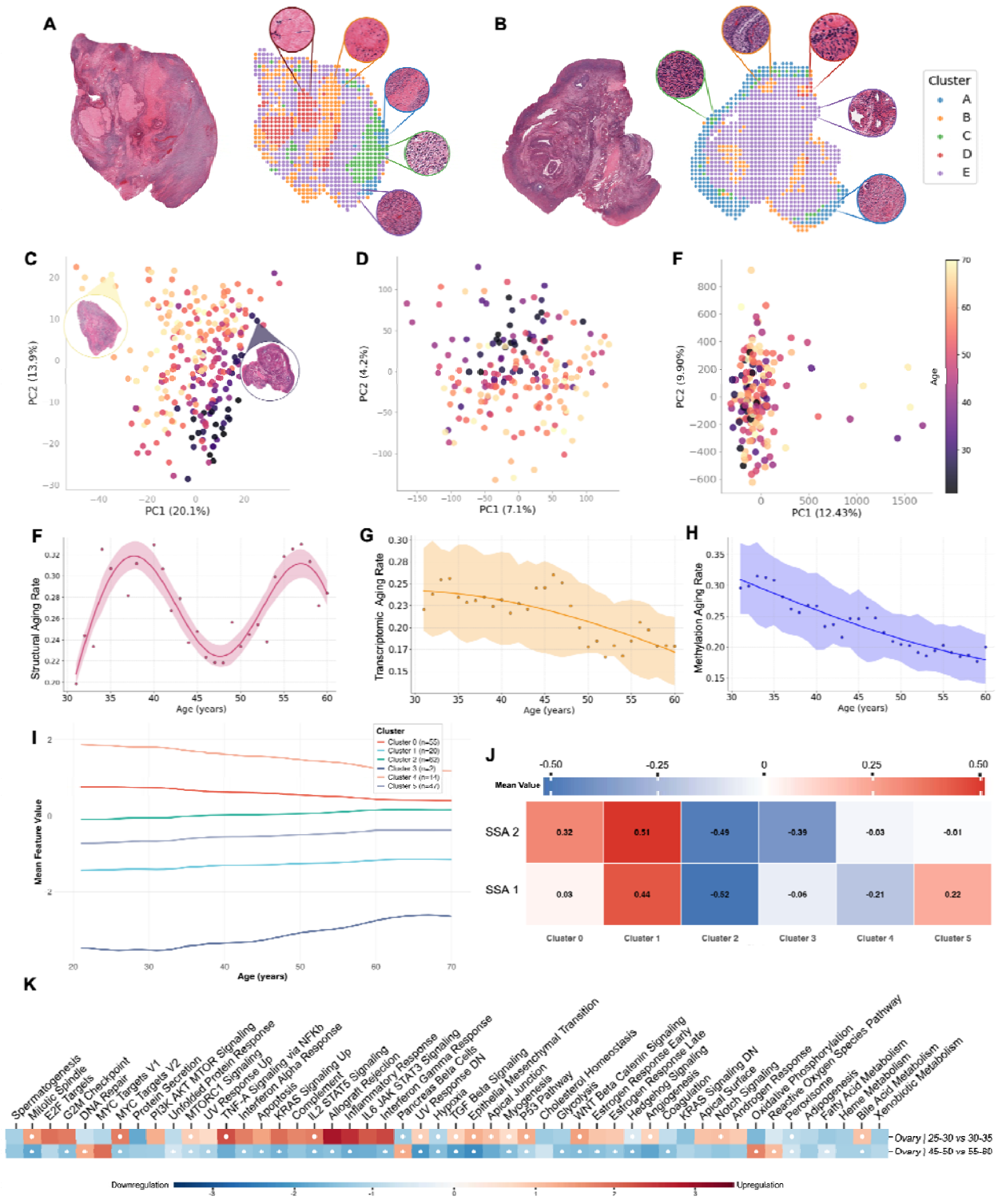

Figure 2: Morphology features capture non-linear ovary structural aging during aging that bulk-molecular profiles cannot. (A-B) *The morphological patch level features from 2 ovary samples from both older (left, age 60-69) and younger (right, age 20-29) clustered show that UNI can very well capture the structural property of the tissue.* **(C-E)** *Principal component analysis of all morphology features*

extracted by UNI in 250 ovary samples from whole slide images separate young vs. old samples, without prior training on chronological age; expression and methylation profiles from the matched samples respectively. **(F)** *PathStAR applied to UNI features from 250 ovarian samples captures non-linear structural aging. The structural aging rate trajectory shows notable peaks at ages 35-40 and 55-60, aligned with established reproductive milestones of fertility decline and menopause.* **(G)** *Expression profiles can segregate young vs. old samples but failed to capture this bimodal structural aging trajectory of ovary.* **(H)** *Methylation profiles fail to capture either young vs. old samples or the structural aging trajectory.* **(I)** *Six different morphological-features modules identified by clustering the top 200 UNI extracted features into 6 clusters, where cluster 0 and 1 showed highest decline with age opposed to cluster 3 which shows increase with age.* **(J)** *Heatmap showing pathway enrichment in ASA 1 and ASA 2 compared to their controls. White dots denote statistically significant enrichment (P < 0.05).*

3.2.3 Molecular Changes During Accelerated Aging Periods of Ovary

We next identified molecular changes during accelerated structural aging by comparing molecular profiles (bulk-expression and methylation) from each ASA period to its preceding structurally stable phase: ASA-1 (35-40 years) vs. baseline (25-30 years), and ASA-2 (55-60 years) vs. baseline (45-50 years). During ASA-1, we observed an upregulation of inflammatory pathways (IFN-gamma response, NFK-Beta signaling, IL6-JAK-STAT3 signaling), cell cycle, and DNA damage response (**Figure 2J, Figure S9**). Further, top pathways silenced due to hypermethylation includes notch signaling (master regulator of granulosa cell proliferation [26, 27]), ERK1/2 (master regulator of both FSH and LH signaling [28,29], **Figure S9**). These changes suggest that ASA-1 reflects a period of pro-inflammatory microenvironment stress, potentially contributing to rapid loss of ovarian reserve [30, 31, 32, 33, 34]. On the other hand, ASA-2 (55-60) (**Figure 2J**), is marked by downregulation of growth factor signaling (EGFR, Wnt) and calcium signaling potentially. This may reflect loss of follicular activity and reduced steroidogenesis, corresponding to post-menopausal period (**Figure 2J**) [35, 36, 37].

Together, above findings shows that PathStAR captured ovary's non-linear decline without chronological age training, enabling the molecular analysis detection of the pathways associated with these structural transitions, which importantly, are not detectable without the preceding structural analysis. These results establish the foundation for whole-body analysis, described next.

3.3 Structural Aging dynamics in different tissues across the whole human body

3.3.1 Morphological Features Segregate Young vs. Old Tissues for Many Tissues Across Body

We next applied PathStAR for the whole human body across 40 tissue types available (N = 970 individuals, N = 25,306 total biopsies, **Methods 5.1**). The morphology-features based PCAs of each tissue is provided in **Figure 3**, where strikingly 15 out of 40

tissues, tissues, without any pretraining on chronological age, can separate young, middle-age and old age samples (regression based on PC1-2 variance explained r^2 >0.15), with the strongest separation in uterus and ovary tissues. We confirmed that this segregation is not driven by number of samples or post-mortem confounders like interval between death and sample collection (ischemic time) in **Notes S3**, **Figure S10**, **Table S1**. This shows that aging substantially remodels these 15 tissues during aging, and that no training is required to separate young vs. old tissues.

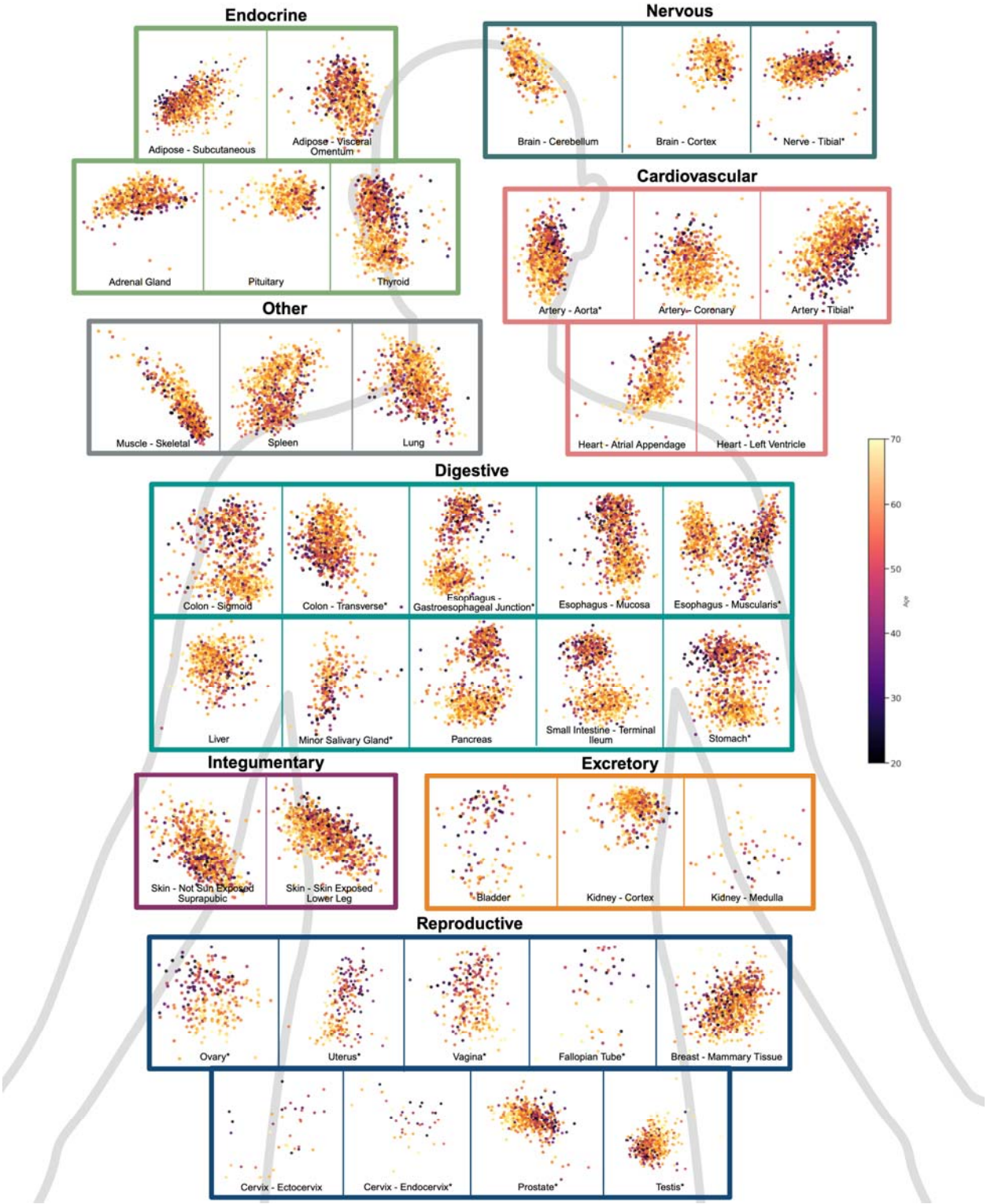

Figure 3: Tissue morphology naturally segregates young vs. old tissues across multiple tissue in human body: *Morphology features-based PCA for 40 tissue types, where darker color represents younger tissue and light colors represents older tissue. Tissues are grouped into their respective organ system outlined in an organ-system specific color. Stars in the name of the tissue represent significant tissues that separate old, middle and young samples without pre-training.*

3.3.2 Human Tissues Age Through at-least Three Distinct Temporal Programs

We generated structural aging rate trajectories for each tissue, selecting only tissues that showed clear morphological differences between young and old samples, indicating detectable structural aging above individual variation. We next filtered and focused on tissue types with high-confidence trajectory (Total N > 200, **Methods 5.2, Notes S6**). This yielded a total of 15 tissues comprising vascular, digestive and reproductive tissues (including ovaries), where we generated remodeling trajectories (**Figure 4A-C**). For transparency, we provide all Raw Data Plots (**Figures R1-R5**) showing individual data points, sample distributions, and sex-stratified analyses.

Structural aging trajectories across these 15 tissues revealed tissue-specific patterns that could be clustered into three groups (**Figure 4A-C, Methods 5.2**). Early-Aging Tissues exhibit high structural aging rates in the 30s where this rate declines later, experiencing high structural changes during young adulthood (**Figure 4A**). Late-Aging Tissues remain structurally stable through early adulthood, then undergo major structural changes in later decades (**Figure 4B**). Biphasic-Aging Tissues display two distinct periods of accelerated structural aging separated by stable phases, like the ovary pattern (**Figure 4C**). Notably, some tissues exhibited markedly higher structural aging rates than others, indicating greater cumulative remodeling over time.

The vascular system, tibial and coronary arteries, showed Early Structural Aging, with structural aging highest in the 30s (**Figure 4D, F**; *Raw points, # of samples/age group & confidence intervals in* **Figure S11**, *Sex-stratified plot in* **R1**). This trajectory is consistent with proteomic studies that also report early cardiovascular aging [38] The trajectory remains consistent even after filtering out individuals with systemic diseases (**Figure R2**). Pathology notes support these findings: 1) Individuals with higher delta-structural aging score is more likely to have atherosclerosis (**Figure S12**); 2) Atherosclerotic changes, early plaque formation in arteries, showed their steepest increase during the 30s vs. 20s, then plateaued in later decades (**Figure S2**, top-left panel). Interestingly, tibial nerve also displays Early Structural Aging, an unexpected finding warranting further investigation.

In contrast, uterus and vagina exhibited Late Structural Aging pattern, with their highest structural aging rates occurring in early and middle 50s **Figure 4E**), aligning with menopause and post-menopause. This likely reflects major changes in uterus including substantial atrophy, endometrial thinning [39], and myometrial structural changes following estrogen withdrawal [40] during menopause and post-menopause [41]. Accelerated structural aging periods of vagina and uterus aligns with ASA-2 of ovary, suggesting coordinated reproductive aging, potentially driven by shared hormonal regulation. We tested this coordination aging at individual-level in next section.

The predominant pattern observed in our dataset was Biphasic Structural Aging, as earlier described for the ovary (Figure 2F), characterized by two distinct peaks of structural aging rates, indicating two periods of accelerated structural aging (**Figure 4C**). While the timing and structural aging rates of two peaks differed among tissue types, this pattern was exhibited by 9 of the 14 tissues examined, including digestive tract (esophagus, stomach, colon, small intestine, salivary gland), male reproductive organs (prostate, testis), and artery-tibial (**Figure 4F**). Overall, the two major periods of accelerated structural aging for these tissues were in the 30s and around the 50s. Beyond sharing similar population-level trajectory, we explored whether digestive tract and male reproductive organs show coordinated structural aging at individual level in next section. Testing contribution of post-mortem artifacts towards these patterns, we find the total variance explained of structural aging rates by all post-mortem artifacts to be minimal in almost all tissues (<10%, **Figure 4G, Table S2-4)**.

Finally, above trajectories do not emerge from molecular age clocks trained on chronological age, which assume linearity by design, nor when applying the same trajectory analysis to bulk expression or methylation profiles (**Figure S13A-C, R4-5**). Overall, this shows that structural aging of human tissues occurs in nonlinear phases rather than gradual decline, with distinct patterns across organ systems: vascular tissues age early (30s), female reproductive tissues coordinate with ovary's late peak (50s), and digestive and male reproductive organs follow a biphasic pattern. Trajectories of 20 additional tissues, with more than 200 biopsies, which were excluded from the main analysis due to not meeting all inclusion criteria are shown in **Figure R3** and trajectory based on transcription and methylation are shown in **Figure R4-5**.

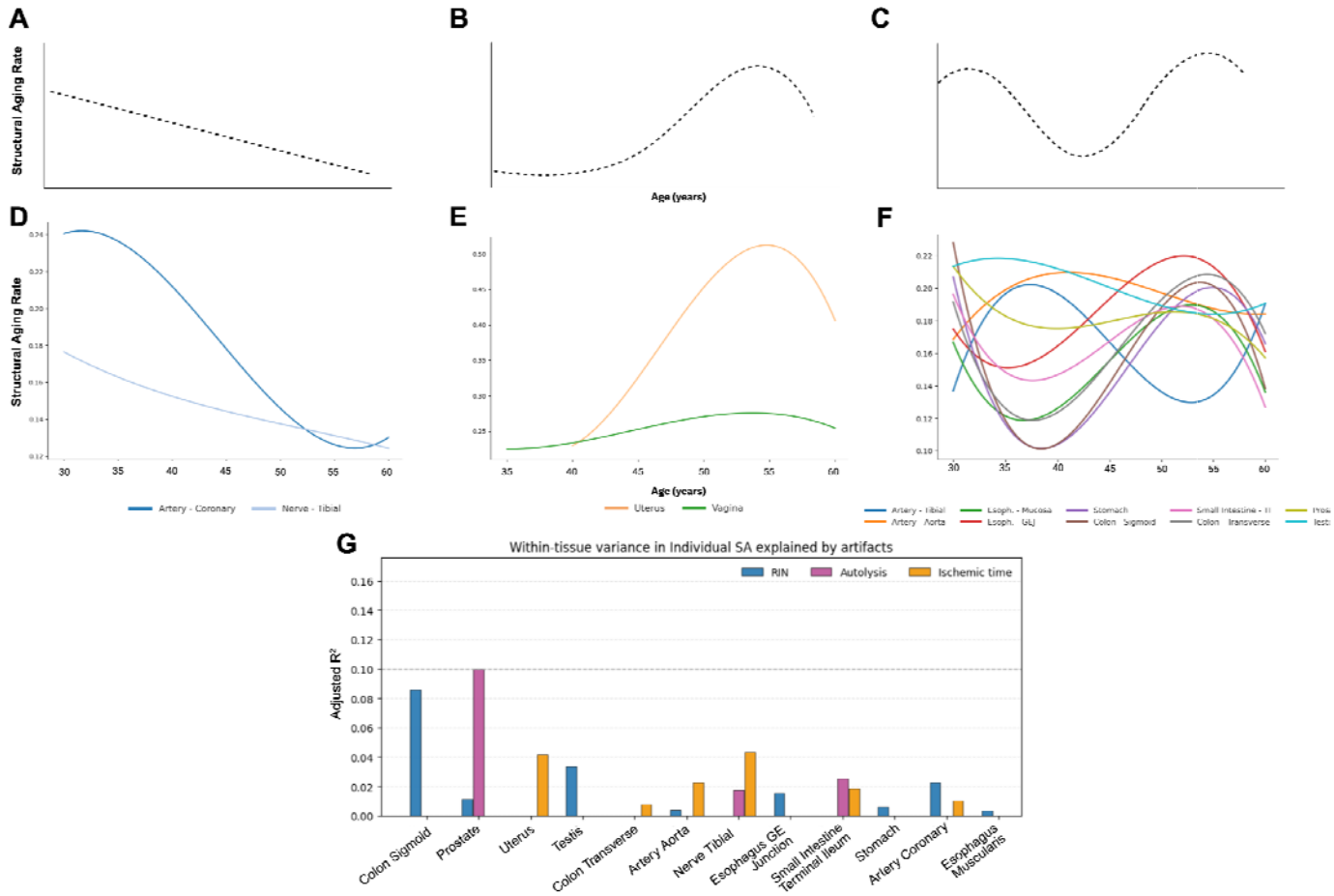

Figure 4: Overview of Structural Aging Trajectories across 14 tissues. (A-C) *Three distinct aging patterns identified: Early Agers peak in the 30s then decline, Late Agers remain stable until major changes in the 50s-60s, and Biphasic Agers (the predominant pattern in 9/14 tissues) exhibit two acceleration periods around the early 30s and 50s.* **(D-F)** *Tissue-specific examples showing vascular and neural tissues as Early Agers, female reproductive tissues as Late Agers, and digestive tract plus male reproductive organs as Biphasic Agers, revealing coordinated aging within functionally related systems.* **(G)** *Within-tissue variance in individual structural age (SA) explained by technical artifacts (RIN, autolysis, ischemic time); except prostate, other tissues show minimal artifact-driven variance.*

3.3.3 Molecular Changes During Accelerated Aging Periods Across Different Tissues

We next identify molecular changes during these ASA periods in each tissue compared to preceding structurally stable phase (**Figure 5A**, data available in **Table S5**). **Figure 5A** provides tissue-specific and age-period-specific molecular changes during accelerated structural deterioration. Illustrating this with one example: Testis showed two ASA periods (ages 35-40 & 45-50). Though the tissues are inflamed in both ASA periods, the spermatogenesis pathway decreased severely during ASA-1 (35-40 yrs) but not in ASA-2 (45-50 yrs) (**Figure 5B**). In contrast, finding pathways that change linearly with age (based on correlation with chronological age) cannot capture this period-specific acute disruption of spermatogenesis (**Figure S14A-B**).

Globally, there were three pattern during ASA-periods across tissues: **1)** Increased inflammation in most tissues (**Figure 5A, *Box I***), in form of upregulation of TNF-alpha via NKFB, Interferon alpha and gamma response, complement pathways; **2)** Decreased Energy Production in most tissues (**Figure 5A, *Box II***), via decreased activity of oxidative phosphorylation pathway; 3) Decreased Ability to Separate Chromosomes for Cell Division (Mitotic Spindle Pathway, **Figure 5A, *Box III***), likely suppressing cell division, across most tissues, but more profoundly in dividing gastrointestinal organs. This decreased was accompanied by downregulation of E2F Targets, G2M checkpoint and MYC-targets pathways. This may act as a protective mechanism against cancer during aging. These three patterns were also overall captured by pathways that linearly change with age (**Figure S14A-B**), but organ-system and tissue-specific unique dysregulation (presented below) were not.

Within organ-systems: **1)** The most distinct molecular change across all arteries is an increase of peroxisome pathways (**Figure 5A, *Box IV***), cellular machinery responsible for fatty acid metabolism, detoxification, and cholesterol processing. This is more severe in second ASA-periods (55-60). This indicates impaired arterial capacity to process lipids and neutralize oxidative damage, contributing to cardiovascular diseases. **2)** Female-reproductive organs, ovary and uterus, showed downregulation of estrogen-response pathway (**Figure 2J, 5A**) during second ASA-period (around menopause time), **3)** Beyond already mentioned inflammation, gastrointestinal tissues (GI) show decreased UV-response-Up pathway (**Figure 5A, *Box V***), a cell response follows up of UV-induced (or other genotoxins) DNA damage and repair. This decrease suggests reduced capacity for DNA damage detection and repair.

Top up/regulated genes and transcriptional factors from one tissue from each trajectory type (nerve-tibial from *early*, uterus from *late* and colon-sigmoid from biphasic) are provided in **Figure S15**. Overall, these molecular changes are correlates of rapid structural aging, where subsets are drivers of organ function decline observed during aging, and some would serve as protective mechanisms against aging-related diseases like cancer.

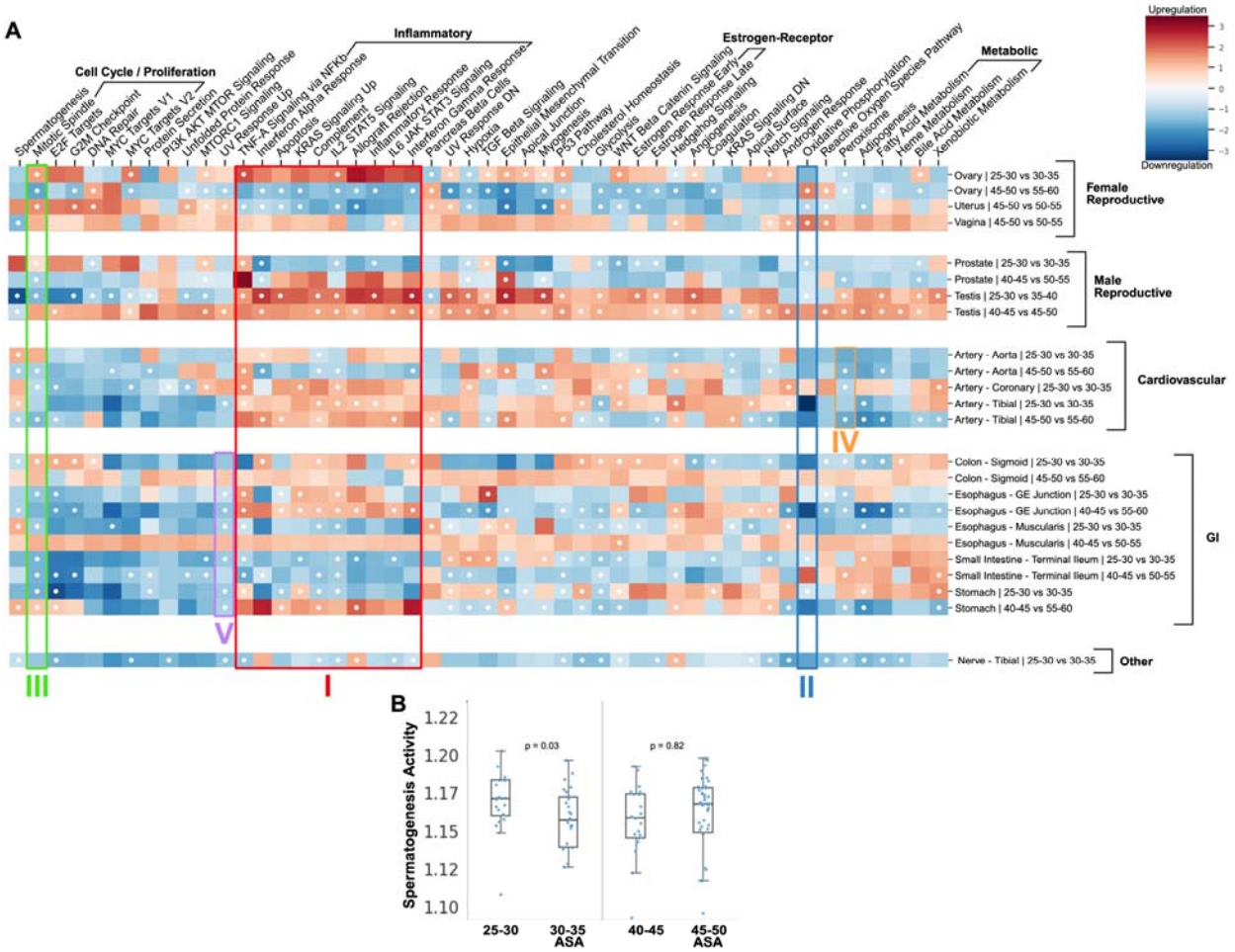

Figure 5: Molecular Changes During ASA in different tissues: ***(A)*** *Heatmap depicting tissue-specific pathway enrichment during periods of accelerated structural aging across female reproductive, male reproductive, cardiovascular, gastrointestinal, and other tissue systems. Rows represent individual pathways within each tissue category; columns represent different age groups (control vs ASA) and tissue types. Color intensity [red – upregulation and blue – downregulation] indicates normalized enrichment scores (NES). White dots denote statistically significant enrichment (P < 0.05). Notable pathways up/down-regulation and tissue groupings are outlined with boxes as following: Box I point the overall increase of inflammation across tissues, II refer to decrease energy production, III refers to decreased ability to segregate chromosome, IV refers to decreased peroxisome activity in arteries, V refers to increased UV-response in GI tissues.* ***(B)*** *Single-sample gene set enrichment analysis (ssGSEA) NES scores for spermatogenesis pathways in testicular tissue, comparing control versus ASA periods across age groups.*

3.4 Cross-organ talk reveal multiple canonical, and novel coordinated multi-organ remodeling axes

Having established tissue-specific structural aging trajectory at the population level, we next investigated whether individuals showing accelerated structural aging in one tissue also exhibit accelerated aging in related tissues—revealing correlated deterioration within the same person. Our study is uniquely powered to investigate this as we have

up to 37 tissues from the same individual, enabling us to ask if higher structural aging in one tissue correlates with more aging in other tissues within the same person.

PathStAR computes individual level delta-Structural Aging scores (ΔSA)(available in **Table S6**) that quantify each tissue's deviation from its corresponding population-level aging trajectory (**Method 5.3**). To identify coordinated aging, we computed correlations among ΔSA scores of the 15 tissues with high-confidence trajectories (**Figure 6, Method 5.7**). Higher positive correlations indicate that individuals with accelerated structural aging in one tissue consistently exhibit accelerated aging in the partner tissue, suggesting synchronized deterioration potentially driven by shared mechanisms. We first observed that multiple tissues from the same organ systems have strong significant positive correlations (**Figure 6A, *Box I-III***). This includes the gastrointestinal system (different parts of colon and esophagus, and stomach, r=0.20-0.43, **Figure 6A, *Box I***), female reproductive system (uterus and vagina, r=0.48, **Figure 6A, *Box II***), and vascular system (artery tibial, artery coronary and artery aorta, r=0.14-0.16, **Figure 6A, *Box III***). When looked at all 40 tissue types, additional within-organ systems coordination, particularly within brain (cerebellum-cortex: r=0.55 in males, 0.40 in females) and cardiac systems emerged (**Figure S16**).

Beyond these canonical within-organ-system correlations, we observed an unexpected cross-system structural aging axis between digestive and reproductive tissues (prostate with colon and esophagus tissues r=0.14-0.43, ***Figure 6A, Box IV***), where if within an individual, accelerated structural aging in digestive organs was associated with accelerated structural aging in prostate. This within-individual coordination aligns with the similar biphasic population-level trajectories these two systems share. Other novel axes include neurovascular coordination (nerve-tibial with multiple arteries, r=0.23-0.28) and sex-specific neuroendocrine coordination (pituitary-brain correlations stronger in males than females).

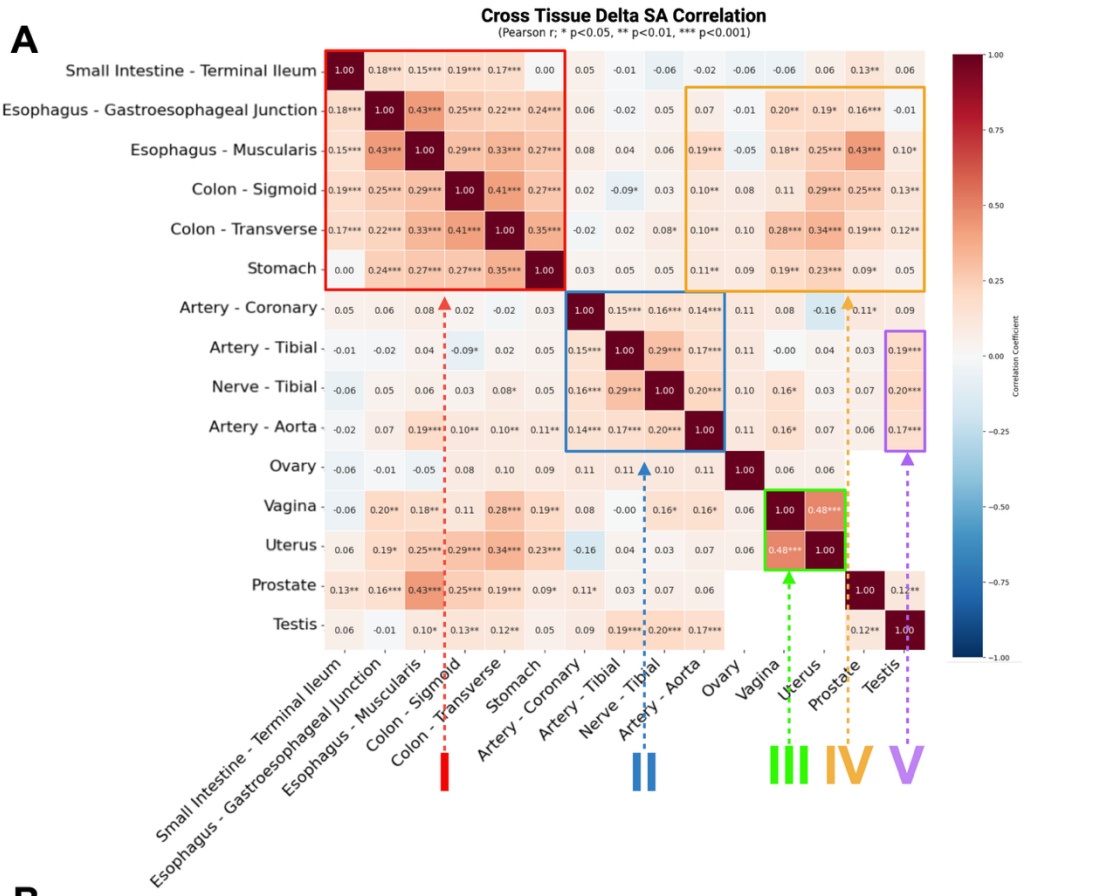
A
Cross Tissue Delta SA Correlation
(Pearson r; * p<0.05, ** p<0.01, *** p<0.001)
Small Intestine - Terminal Ileum
Esophagus - Gastroesophageal Junction
Esophagus - Muscularis
Colon - Sigmoid
Colon - Transverse
Stomach
Artery - Coronary
Artery - Tibial
Nerve - Tibial
Artery - Aorta
Ovary
Vagina
Uterus
Prostate
Testis
Correlation Coefficient
I
II
III
IV
V

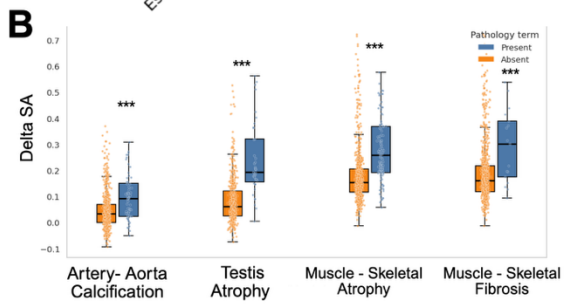
B
Delta SA
Pathology term
Present
Absent
Artery- Aorta Calcification
Testis Atrophy
Muscle - Skeletal Atrophy
Muscle - Skeletal Fibrosis

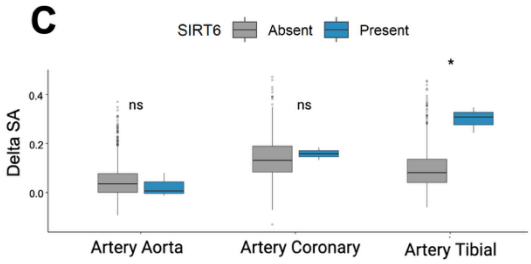
C
SIRT6
Absent
Present
Delta SA
ns
ns
*
Artery Aorta
Artery Coronary
Artery Tibial

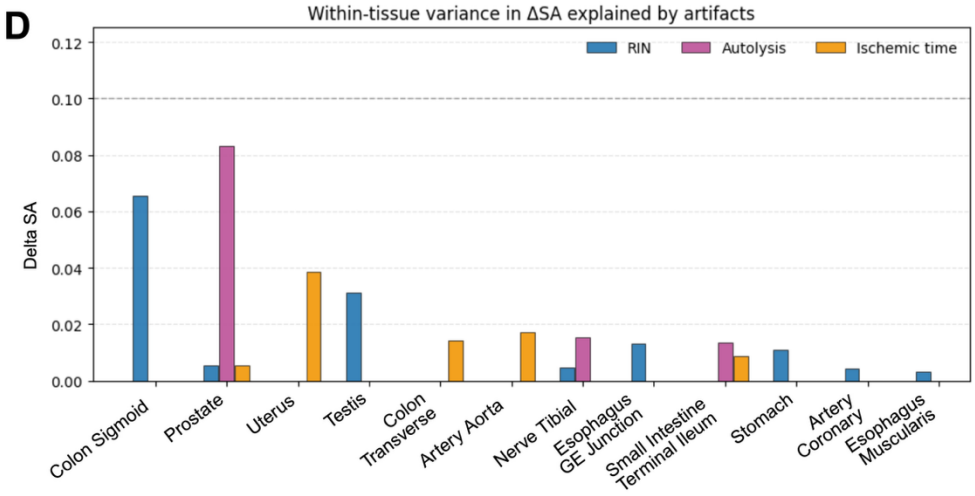
D
Within-tissue variance in ΔSA explained by artifacts
RIN
Autolysis
Ischemic time
Delta SA
Colon Sigmoid
Prostate
Uterus
Testis
Colon Transverse
Artery Aorta
Nerve Tibial
Esophagus GE Junction
Small Intestine Terminal Ileum
Stomach
Artery Coronary
Esophagus Muscularis

Figure 6: Cross-tissue Delta-Structural Aging score correlations reveal coordinated structural aging within individual. (A)*. Heatmap showing Pearson correlation coefficients between individual Delta-Structural Aging (SA) scores across 15 tissue types from the same individuals (n=970). Delta-SA scores quantify each individual's deviation from expected structural aging trajectories for each tissue. Color scale represents correlation strength: dark red indicates strong positive correlations (r≥0.4), light red/orange indicates moderate positive correlations (r=0.2-0.4), white indicates weak correlations (r<0.2), and blue indicates negative correlations. Strong positive correlations reveal coordinated aging between tissue pairs, where individuals with accelerated structural aging in one tissue consistently exhibit accelerated aging in the partner tissue, suggesting synchronized deterioration driven by shared mechanisms. The p-values reported are before FDR-correction. (**B)** Box plot showing the distribution of delta SA score in calcification present and absent in artery aorta, atrophy present and absent in testis and muscle, fibrosis in muscle (p value for *** < 0.001) **(C)** Distribution of Delta SA score in Artery- Aorta, coronary and tibial with SIRT6 present and absent**.** p value for * < 0.05) **(D)** Within-tissue variance in ΔSA across age groups attributable to artifacts. The variance explained is uniformly low, suggesting remodeling dynamics are not driven by technical confounders.*

3.5 Clinical and Genetic Determinants of Organ-Specific Structural Aging

To identify modifiable factors and genetic determinants of accelerated structural aging, we tested associations between individual-level Delta-SA scores and clinical health records, lifestyle factors, and germline variants. Controlling for post-mortem artifacts using a multivariate regression, we found that accelerated structural aging showed strong positive associations with canonical aging pathologies (**Figure S16A** *showing all association*) including atrophy (**Figure 6B**, broad associations across tissues, particularly strong in gastrointestinal and reproductive systems), fibrosis, calcification (in vascular system), and hyalinization. Among systemic diseases, autoimmune conditions such as Lupus and neurological diseases like Dementia showed positive associations across multiple tissues, validating that individuals with these conditions exhibit globally accelerated structural aging (**Figure S17A**). Lifestyle variables had insufficient sample sizes to reach statistical significance for any association tests after FDR correction (**Figure S18**).

We next performed genome-wide association analysis between germline variants of 970 individuals and Delta-SA scores (**Methods 5.9**). We focused on 127K variants (functional variants filtered from Starting 998K variants) where a total of 123 genes showed significant associations with Delta-SA scores (FDR P<0.1, **Figure S17B, 19**).

Our most striking discovery was that SIRT6 variants are specifically associated with accelerated vascular structural aging (**Figure 6C**). SIRT6 encodes a NAD+-dependent deacetylase, previously noted as master regulator of cellular longevity by regulating DNA repair, telomere maintenance, and metabolic homeostasis. Previous studies have implicated SIRT6 in vascular health through, where KO mice showed early atherosclerosis.[42] This represents the first evidence linking genetic variation in a prior

longevity regulator to organ-specific structural aging patterns, demonstrating that certain aging pathways have tissue-selective effects rather than uniform whole-body impacts. The complete 123 variants are available in **Table S7** for the community. Detrimental variants accelerating structural aging are enriched in genes from oxidative phosphorylation and mitochondrial function and protective variants are enriched in immune signaling pathways, particularly IL17 and interferon signaling (**Figure S20**).

Conclusion

This study challenges the prevailing view of aging as a gradual, uniform process established by widespread use of aging molecular clocks trained on chronological age, revealing that when aging is measured through tissue structure rather than molecular proxies of chronological age, it unfolds in discrete, non-linear phases of accelerated change with tissue-specific molecular changes, with distinct tissue-specific trajectories. We further demonstrate that structural aging follows predictable multi-organ coordination patterns within individuals, with unique molecular signatures and with genetic variants like SIRT6 exerting tissue-selective rather than whole-body effects, providing a path for personalized organ-specific aging risk prediction. We establish PathStAR as a framework to study structural aging as a new window into aging biology.

4. Discussion

We developed PathStAR, the first computational framework to systematically quantify structural aging across human tissues from routine histopathology asking when and how they change. This revealed tissue-specific aging trajectories with three distinct patterns: Early Agers (vascular system peaking in 30s), Late Agers (female reproductive tissues peaking around menopause), and Biphasic Agers (digestive and male reproductive tissues with two acceleration periods). This structural lens provides a fundamentally new window into aging biology, demonstrating how tissue architecture—the physical foundation of organ function—deteriorates through discrete phases rather than gradual decline. Challenging the prevailing model of aging as a gradual, steady deterioration process, our findings establish a paradigm of non-linear, tissue-specific structural aging coordinated across organ-systems and within individual, accompanied by distinct molecular pathway dysregulation during these periods.

These tissue-specific aging patterns potentially reflect distinct functional demands and regulatory mechanisms of different organ systems. Early vascular aging aligns with cardiovascular disease pathogenesis, where atherosclerotic changes begin in young adulthood. Female reproductive tissues coordinated late aging around menopause demonstrates hormonal regulation as a master coordinator, where estrogen withdrawal triggers synchronized architectural changes. The predominant biphasic pattern in

digestive and male reproductive organs suggests two critical vulnerability windows, potentially reflecting shared regulatory pathways. Most striking was coordinated structural aging within individuals—while expected coordination within organ systems confirmed functional interdependence, the novel and unexpected coordination between digestive and male reproductive tissues suggests unknown impactful systemic players to uncover.

We also revealed molecular dysregulated programs during accelerated structural aging periods – both pan-tissue and tissue-specific ones. Notable global ones are increased inflammation and decreased metabolic power generation. These are also the major pathways captured when probing for pathways linearly up/down during aging. However, multiple tissues ASAs were unique, prostate (25-30), both ASAs of ovary, testis, and more, and studying it further will reveal targets to preserve deterioration during these periods.

The discovery that SIRT6 variants specifically accelerate vascular structural aging represents a shift from universal aging genes to tissue-selective genetic effects, challenging the assumption that longevity regulators uniformly impact all tissues. This possibly explains the heterogeneity of aging processes observed in human populations even within the same geographical region. This suggests that instead of one-size-fits-all healthy aging dietary and lifestyle approaches, polygenic score-based predictions of tissue-specific structural aging trajectories could enable more targeted interventions—for example, individuals with higher vascular aging risk would benefit from early cardiovascular-focused interventions, while those with accelerated reproductive aging risk would prioritize hormone-related protective strategies.

Several methodological limitations warrant consideration in interpreting these biological insights spanning feature extraction, temporal resolution, data heterogeneity, and interpretability. Our approach generates slide-level embeddings through mean pooling across all patches, representing a relatively blunt aggregation method that could be considerably improved through more sophisticated attention-based or hierarchical pooling strategies. The temporal resolution of our analysis is constrained by available data points in each age group, necessitating a sliding window approach with 10-year increments that may obscure finer structural transitions occurring at narrower time intervals. The GTEx dataset's inherent heterogeneity—comprising tissues from donors with diverse clinical backgrounds including ventilator cases and varying postmortem intervals—introduces potential confounding variables that could influence structural assessments beyond chronological aging effects. Finally, our reliance on deep-learning morphological features leaves multiple structural patterns during aging with limited biological interpretability and developing more interpretable feature extraction methods

that directly map to known histological patterns would significantly advance the framework's clinical utility and biological understanding.

Our structural aging lens provides a fundamentally new window into aging biology. As the physical structure of tissue is the basis of its function, structural aging offers a more interpretable connection to functional decline during aging than molecular approaches alone. Our hope is that it will lay the basis for assessing anti-aging intervention efficacy by quantifying whether treatments preserve tissue architecture and connecting tissue structural patterns to blood-based biomarkers for non-invasive aging monitoring. Additionally, it may enable to assess the structural effects of different drugs currently in use on different tissues, and the association of drug toxicities and adverse effects with rapid structural alterations in different tissues. In closing, by establishing structural aging as a quantifiable and predictable process, PathStAR opens a new, structural dimension for aging research.

5. Methods

5.1 Data Acquisition

Whole-slide images were obtained from the GTEx public portal via v10 release (https://www.GTExportal.org/home/). All slides were digitized at 20X magnification (~0.5 microns per pixel) using an Aperio scanner (SVS format). Protected data, including participant demographic information (chronological age), lifestyle factors, clinical information, and gene expression data, were accessed through dbGAP (Request accession ID: 39103) (20).

5.2 Dataset Selection and Filtering

While the GTEx project encompasses samples from 54 different tissues collected from nearly 1,000 adult post-mortem donors, we focused our analysis on a subset of tissues based on two key criteria: 1) Availability of H&E-stained tissue images, 2) Number of samples >200 for robust modeling. The threshold of at least 200 samples provides enough data to capture the robust age-related changes in different age groups.

5.3 PathStAR Pipeline

Using above filtrated GTEx data, we developed PathStAR pieline comprising the following three steps:

i. Preprocessing of WSI and Feature Extraction: We implement the vision encoder UNI for WSI feature extraction. UNI gives patch level embeddings that we then aggregate to create whole slide representations. UNI is a large vision transformer (ViT), pre-trained using the state-of-the-art self-supervised learning algorithm DINOv2[X] - a student-teacher knowledge distillation for ViT architecture. UNI was pretrained on the Mass-

100K dataset, a dataset containing more than 100 million tissue patches across 20 major tissue types. To preprocess whole slide images for UNI, we implemented Sobel edge detection to first identify regions of the slide containing tissue. Each 20x magnification WSI was then segmented into 512 x 512-pixel patches. Patches were excluded if more than 50% of their pixels exhibited low weighted gradient magnitude, as determined by Sobel. RGB color normalization was applied to remaining tiles using Macenko's. Following image preprocessing, these patches are passed to UNI to extract 1024-dimension patch level features. We create a whole slide representation by aggregating each 1,024-patch level feature together by taking mean across the patches for each feature giving us a final output of 1024 vectors.

ii. Quantifying Remodeling Rate: To identify age-related remodeling rate in each tissue, we developed a sliding window analysis framework that quantifies effect sizes while stratifying by biological sex. For each tissue type with ≥200 samples, we implemented a comparative analysis between age-adjacent windows. For a given window size w (primarily using w=10 years) and target age t, we compared the 1024 slide level features from UNI, in the lower window [t-w, t-1] with those in the upper window [t, t+w-1]. This analysis was restricted to valid age ranges ($t \in$ [min_age+w, max_age-w]) to ensure complete windows.

For each feature dimension i ($1 \leq i \leq 1024$), we calculated total change in the whole-slide morphology vector and the overall effect size as:

$$\text{Remodeling Rate} = \sum_{i=1}^{1024} d_i$$

Statistical significance was assessed using Welch's t-test with significance threshold α=0.05. We defined significant age transitions as those where ≥5% of features showed statistically significant changes after testing. For visualization and analysis, we computed the mean absolute effect size across all features for each target age.

Filtering Remodeling Data points with low statistical Confidence: We only considered age points with sufficient samples (n≥10) in both lower and upper windows and only these were included in the analysis. All analyses were conducted together and then separately for male and female samples to identify sex-specific aging patterns. This approach enabled identification of critical age thresholds where substantial morphological remodeling occurs across different tissue types and biological sexes.

Generating Remodeling Trajectory: Smoothing remodeling rates across all age points, we developed remodeling trajectory in each tissue type by smoothening the datapoints using Spline and Gaussian Smoothening. For spline smoothing, we used Univariate Spline with a smoothing parameter calculated as s = (window size / n) × 0.5 × n, where window size = 10. The Gaussian process utilized RBF kernels with length scales

proportional to window size for comparable smoothing behavior. Then one with best fit was chosen for the tissue type.

iii. *Individual Level Tissue Score:*

A sliding window approach was implemented to quantify morphological deviations within tissue-specific contexts. For each target sample *i* with age $\mathrm{ai} \geq 30$ years, a reference group Ri was defined using the morphological remodeling rate of the same tissue type in the window: $[ai - 10, ai - 1]$

An effect size metric was defined to quantify the deviation in morphological remodeling rate magnitude between target samples and their age-matched reference populations. For each feature dimension j , the effect size was computed as the absolute mean difference:

$$\mathrm{ES}_j = \left|x_{i,j} - \mu_{R_i,j}\right|$$

Where $x_{i,j}$ represents the j-th feature dimension of the target sample i , and $\mu_{R_i,j}$ is the mean of the j -th feature across the reference group R_i. This effect size metric captures the absolute magnitude of morphological deviation without normalization by reference group variability, providing a direct measure of the morphological distance between target samples and their younger counterparts. The final effect size for each target sample was computed as the mean across all p feature dimensions:

$$\mathrm{ES}_i = \frac{1}{p}\sum_{j=1}^{p}\left|x_{i,j} - \mu_{R_i,j}\right|$$

The effect size provides an interpretable measure of morphological changes, with larger values indicating greater deviation from the typical morphology of individuals within the same tissue.

5.4 Identifying pathways up/down regulated during major remodeling periods

We developed a comparison framework to identify the key pathways up/down regulated during major remodeling periods. The key to this was utilizing paired transcriptomics and methylation data from the same biopsies available at GTEx Portal. We identified pathways up/downregulated during ASA1 by comparing the expression profile of samples from ASA 1 with the 5 age periods where accelerated Structural Aging graph shows inflection point. Gene expression profiles were filtered to include only protein-coding genes based on established gene symbols. Expression values for each gene were extracted for both sample groups, and genes with missing data in either group

were excluded from analysis. Statistical significance was assessed using Welch's two-sample t-test, with log2 fold changes calculated as log2(mean_group2 + 1e-5) - log2(mean_group1 + 1e-5) to avoid division by zero. All genes from the differential expression analysis were ranked by log2 fold change in descending order and subjected to Gene Set Enrichment Analysis (GSEA) using GSEApy against the [pathway database] with 10,000 permutations. Pathways with false discovery rate (FDR) q-value < 0.1 and absolute normalized enrichment score (|NES|) > 1.5 were considered significantly enriched.

Above analysis was repeated for methylation, also downloaded from GTEx portal, separately for hypermethylated and hypomethylated states._Gene Set Enrichment Analysis (GSEA) was performed using the GSEApy package with pre-ranked gene lists derived from differential expression results. Pathway enrichment was assessed against multiple curated gene set collections from the Molecular Signatures Database (MSigDB), including KEGG pathways, Gene Ontology (GO) terms, and the C3 collection containing transcription factor targets (TFT).

5.5 Cluster the ovary feature changes with age to find modules

To identify age-informative feature modules in ovary tissue, we employed a two-stage approach combining mutual information (MI) feature selection with K-means clustering. Mutual information between each feature and continuous chronological age was calculated using k-nearest neighbor density estimation, which directly handles continuous age values without discretization. Features with higher MI scores indicate stronger association with age-related changes. The top 200 features with highest MI scores were selected and subsequently clustered using K-means clustering after z-score normalization to ensure equal weighting across features with different expression ranges. Clustering was performed across multiple K values (4, 5, 6, 9, 12, 15, and 20) with K-means initialization and fixed random seed (42) for reproducibility. Each resulting cluster represents co-regulated features exhibiting similar trajectories.

5.6 Mechanistic Interpretation of Morphological Features using vision language models

To interpret morphological features extracted by UNI, we employed two state-of-the-art vision-language models: PLIP. PLIP leverages contrastive learning on paired pathology images and diagnostic text to learn clinically relevant representations, while Conch, developed by the Mahmood laboratory, specializes in histopathological image understanding through self-supervised learning on large-scale tissue collections.
We established interpretability baselines by computing patch-level semantic similarity scores via dot product operations between patch embeddings and a curated vocabulary of 500 terms, comprising 10 ovary-specific descriptors, 240 general pathological terms, and 250 common English words. Slide-level similarity scores were derived by

aggregating patch-level scores using the 95th percentile to capture the most relevant morphological patterns.

Three complementary analyses were performed: (1) validation against ground truth annotations from GTEx pathology reports to assess model accuracy, (2) correlation analysis between similarity scores and chronological age for ovary-specific features including follicular structures, stromal fibrosis, and tissue atrophy, and (3) comparative analysis of pathological features during the menopausal transition period. This multimodal approach enabled quantitative interpretation of morphological changes while maintaining clinical relevance and biological plausibility.

5.7 Cross-Tissue Aging Correlation Analysis

To compute cross-tissue co-ordination in remodeling during aging, we computed correlations between accelerated remodeling or delta remodeling scores (denoted as ΔSA) using using Pearson's correlation coefficients among organs implemented in SciPy. For each tissue pair, individuals with missing data in either tissue were excluded from the correlation calculation to maintain paired observations. Pairwise correlations were computed for ΔSA across all possible tissue combinations, generating both correlation coefficients and associated p-values. A minimum threshold of 10 paired observations was required for correlation calculations to ensure meaningful statistical inference. Statistical significance was assessed at three levels: $p < 0.05$, $p < 0.01$, and $p < 0.001$.

5.8 Disease and Lifestyle Association with Accelerated Remodeling

We tested three categories of clinical features for their association with delta remodeling scores (ΔSA): (1) pathology terms extracted from histopathological reports, (2) Hardy Scale death classifications, and (3) binary disease history indicators from phenotypic metadata. For pathology terms, we applied text mining approaches to identify the presence or absence of specific pathological conditions within clinical notes and structured pathology categories for each sample.

Statistical associations were evaluated using multiple linear regression to control for ischemic time as a potential confounding variable. The regression model was specified as: ΔSA ~ clinical feature + ischemic time + intercept, where clinical feature represents the binary indicator (presence/absence) of each pathological condition, Hardy Scale comparison, or disease history. Missing ischemic time values were imputed as zero to maximize sample retention while maintaining analytical rigor. For each clinical feature, we extracted regression coefficients, p-values, and R^2 values to quantify the magnitude and significance of associations after controlling for ischemic time effects.

Hardy Scale comparisons were performed systematically across six predefined death circumstance pairs (e.g., violent vs. slow death, intermediate vs. slow death), while disease features compared individuals with and without specific medical histories from

the top 20 most prevalent conditions. All pathology terms identified through text mining were tested comprehensively rather than limiting to high-frequency terms. To address multiple testing, we applied Bonferroni correction both within tissues and globally across all comparisons. Only associations with adequate sample sizes (≥10 samples per group) were included in the analysis to ensure statistical power for regression modeling.

5.9 Germline Association with Delta SA

We processed the multi-sample GTEx whole-exome sequencing (WES) variant call file (VCF), which contains 979 individuals with variant genotypes and functional annotations. From this file we extracted three layers of information: (i) the core variant descriptors (chromosome, position, reference and alternate alleles, quality, and filter status); (ii) annotation fields from the INFO column, including allele frequency, allele count, quality metrics, and VEP-derived functional annotations such as predicted consequence, impact, gene symbol, and clinical significance; and (iii) individual-level genotypes for each sample, standardized into categorical calls (homozygous reference, heterozygous, homozygous alternate, or missing). This parsing produced structured variant-level tables in which each row corresponded to a single variant, annotated with both functional attributes and per-sample genotypes.

For each tissue, all variants were grouped by gene symbol, and a gene burden score was calculated for every individual by summing the genotypes across all variants mapping to that gene. We also recorded gene-level metadata including the chromosome assignment and the number of variants contributing to each gene's burden. Gene burden scores were then associated with patient-specific delta SA scores using linear regression of the form:

$$\text{delta SA score} = \beta \times \text{gene burden} + \varepsilon$$

From each model we extracted the slope (β), standard error, p-value, coefficient of determination (R^2), and correlation coefficient. The resulting tissue-specific association tables contained, for every gene, the number of contributing variants, number of samples analyzed, and full regression statistics. Multiple-testing correction was applied using the Benjamini–Hochberg false discovery rate procedure, and both complete and significant results were retained.

5.10 Molecular Clock

5.10.1 Transcriptomic molecular clock

We trained tissue-specific transcriptomic clocks to predict chronological age from bulk RNA-seq data in GTEx. For each tissue, expression matrices (log-transformed TPMs) were processed after collapsing technical replicates to a single donor-level profile, retaining samples with ≥100 individuals. Within each training fold, genes were pre-filtered by correlation with age, and the top 3,000 most age-associated features (by absolute Pearson correlation) were retained. Features were standardized (z-scored)

within the training set, and age prediction models were trained using an elastic net regression framework. Regularization hyperparameters (α across 18 log-spaced values and l1_ratio ∈ {0.1, 0.5, 0.9}) were tuned internally by five-fold cross-validation. To avoid information leakage, feature selection and scaling were repeated independently within each fold, and folds were defined by GroupKFold stratification over donor IDs to ensure that multiple samples from the same individual did not cross training–validation boundaries.

Performance was assessed in each fold using mean absolute error (MAE, in years) and coefficient of determination (R^2).

5.10.2 Methylation molecular clock

We trained tissue-specific clocks to predict chronological age from DNA methylation profiles. For each tissue with ≥100 samples, methylation matrices and aligned metadata (age, donor ID) were loaded, and feature selection was performed within each cross-validation fold to avoid leakage. In each fold, CpGs were ranked by their absolute Pearson correlation with age, and the top 2,000 sites were retained. Selected features were standardized using training statistics, and age was predicted using elastic net regression with hyperparameters tuned by internal cross-validation (α across 12 log-spaced values; l1_ratio ∈ {0.1, 0.9}). Donor IDs were used as grouping factors in five-fold cross-validation, ensuring samples from the same individual did not cross training–validation boundaries.
Performance was assessed in each fold using mean absolute error (MAE, in years) and coefficient of determination (R^2).

6. Data Availability Statement

The data used in this study were obtained from the Genotype-Tissue Expression (GTEx) Project (accession: phs000424.v10.p2, Project titled #39103). The H&E histological images and transcriptomic data are publicly available and were accessed through the GTEx Portal v10 release (https://GTExportal.org/home/). The germline variant data, phenotype and metadata, e.g. age, lifestyle factors etc. were extracted after appropriate institutional approval and data access agreement (General Research Use: phs000424.v10.p2.c1). The mean-pooled features generated from GTEx histology images using the UNI foundational model have been deposited on Zenodo(link).

7. Code Availability

PathStAR is available on GitHub as a software package for academic use. The complete source code and documentation can be accessed at: https://github.com/Sinha-CompBio-Lab/PathStAR.git

8. Conflict Of Interest

AY. And S.S. have filed a provisional patent related quantifying structural aging rate from H&E images.

9. Authors Contribution

S.S. conceived and designed the study to quantify morphological changes in tissue using hematoxylin and eosin (H&E) histological images. A.Y. developed the computational framework and implemented the PathStAR pipeline for automated quantification of tissue morphological changes from H&E-stained slides. A.Y. performed validation analyses and computational benchmarking of the PathStAR methodology. K.A. prepared visual presentations of the data and performed some of the analysis. A.Y. drafted the initial manuscript. S.S. provided critical manuscript revisions and supervised the research. K.Y and C.K helped in biological interpretation of structural aging rates and trajectories.

10. Acknowledgements

This research was supported by the Sanford Burnham Prebys NCI-designated Cancer Center Start-up Fund for Sinha Lab. We thank Peter Adams for feedback on the manuscript.

11. References

[1] Niccoli T, Partridge L. Ageing as a risk factor for disease. Curr Biol. 2012 Sep 11;22(17):R741-52. doi: 10.1016/j.cub.2012.07.024. PMID: 22975005.

[2] Guo, J., Huang, X., Dou, L. et al. Aging and aging-related diseases: from molecular mechanisms to interventions and treatments. Sig Transduct Target Ther 7, 391 (2022). https://doi.org/10.1038/s41392-022-01251-0

[3] Wang S, Huo T, Lu M, Zhao Y, Zhang J, He W, Chen H. Recent Advances in Aging and Immunosenescence: Mechanisms and Therapeutic Strategies. Cells. 2025 Mar 27;14(7):499. doi: 10.3390/cells14070499. PMID: 40214453; PMCID: PMC11987807

[4]Li Y, Tian X, Luo J, Bao T, Wang S, Wu X. Molecular mechanisms of aging and anti-aging strategies. Cell Commun Signal. 2024 May 24;22(1):285. doi: 10.1186/s12964-024-01663-1. PMID: 38790068; PMCID: PMC11118732.

[5] Levine ME, Lu AT, Quach A, Chen BH, Assimes TL, Bandinelli S, Hou L, Baccarelli AA, Stewart JD, Li Y, Whitsel EA, Wilson JG, Reiner AP, Aviv A, Lohman K, Liu Y, Ferrucci L, Horvath S. An epigenetic biomarker of aging for lifespan and healthspan. Aging (Albany NY). 2018 Apr 18;10(4):573-591. doi: 10.18632/aging.101414. PMID: 29676998; PMCID: PMC5940111.

[6] Lu AT, Quach A, Wilson JG, Reiner AP, Aviv A, Raj K, Hou L, Baccarelli AA, Li Y, Stewart JD, Whitsel EA, Assimes TL, Ferrucci L, Horvath S. DNA methylation GrimAge strongly predicts lifespan and healthspan. Aging (Albany NY). 2019 Jan 21;11(2):303-327. doi: 10.18632/aging.101684. PMID: 30669119; PMCID: PMC6366976.

[7] Shen, X., Wang, C., Zhou, X. et al. Nonlinear dynamics of multi-omics profiles during human aging. Nat Aging 4, 1619–1634 (2024). https://doi.org/10.1038/s43587-024-00692-2

[8] Schaum, N., Lehallier, B., Hahn, O. et al. Ageing hallmarks exhibit organ-specific temporal signatures. Nature 583, 596–602 (2020). https://doi.org/10.1038/s41586-020-2499-y

[9] Sherratt MJ. Age-Related Tissue Stiffening: Cause and Effect. Adv Wound Care (New Rochelle). 2013 Feb;2(1):11-17. doi: 10.1089/wound.2011.0328. PMID: 24527318; PMCID: PMC3840474.

[10] Bonta M, Daina L, Mețiu G. The process of ageing reflected by histological changes in the skin. Rom J Morphol Embryol. 2013;54(3 Suppl):797-804. PMID: 24322030.

[11] Wilkinson DJ, Piasecki M, Atherton PJ. The age-related loss of skeletal muscle mass and function: Measurement and physiology of muscle fibre atrophy and muscle fibre loss in humans. Ageing Res Rev. 2018 Nov;47:123-132. doi: 10.1016/j.arr.2018.07.005. Epub 2018 Jul 23. PMID: 30048806; PMCID: PMC6202460.

[12] Zeisberg M, Kalluri R. Cellular mechanisms of tissue fibrosis. 1. Common and organ-specific mechanisms associated with tissue fibrosis. Am J Physiol Cell Physiol. 2013 Feb 1;304(3):C216-25. doi: 10.1152/ajpcell.00328.2012. Epub 2012 Dec 19. PMID: 23255577; PMCID: PMC3566435.

[13] Umehara T, Richards JS, Shimada M. The stromal fibrosis in aging ovary. Aging (Albany NY). 2018 Jan 19;10(1):9-10. doi: 10.18632/aging.101370. PMID: 29356685; PMCID: PMC5811253.

[14] Piemontese M, Almeida M, Robling AG, Kim HN, Xiong J, Thostenson JD, Weinstein RS, Manolagas SC, O'Brien CA, Jilka RL. Old age causes de novo intracortical bone remodeling and porosity in mice. JCI Insight. 2017 Sep 7;2(17):e93771. doi: 10.1172/jci.insight.93771. PMID: 28878136; PMCID: PMC5621920.

[15] Marcus RL, Addison O, Kidde JP, Dibble LE, Lastayo PC. Skeletal muscle fat infiltration: impact of age, inactivity, and exercise. J Nutr Health Aging. 2010 May;14(5):362-6. doi: 10.1007/s12603-010-0081-2. PMID: 20424803; PMCID: PMC3758242.

[16] Biernacka A, Frangogiannis NG. Aging and Cardiac Fibrosis. Aging Dis. 2011 Apr;2(2):158-173. PMID: 21837283; PMCID: PMC3153299.

[17] Yu HX, Feng Z, Lin W, Yang K, Liu RQ, Li JQ, Liu XY, Pei M, Yang HT. Ongoing Clinical Trials in Aging-Related Tissue Fibrosis and New Findings Related to AhR

Pathways. Aging Dis. 2022 Jun 1;13(3):732-752. doi: 10.14336/AD.2021.1105. PMID: 35656117; PMCID: PMC9116921.

[18] Tracy E, Rowe G, LeBlanc AJ. Cardiac tissue remodeling in healthy aging: the road to pathology. Am J Physiol Cell Physiol. 2020 Jul 1;319(1):C166-C182. doi: 10.1152/ajpcell.00021.2020. Epub 2020 May 20. PMID: 32432929; PMCID: PMC7468888.

[19] Gui J, Mustachio LM, Su DM, Craig RW. Thymus Size and Age-related Thymic Involution: Early Programming, Sexual Dimorphism, Progenitors and Stroma. Aging Dis. 2012 Jun;3(3):280-90. Epub 2012 Mar 14. PMID: 22724086; PMCID: PMC3375084.

[20] Pescosolido N, Barbato A, Giannotti R, Komaiha C, Lenarduzzi F. Age-related changes in the kinetics of human lenses: prevention of the cataract. Int J Ophthalmol. 2016 Oct 18;9(10):1506-1517. doi: 10.18240/ijo.2016.10.23. PMID: 27803872; PMCID: PMC5075670.

[21] GTEx Consortium. The Genotype-Tissue Expression (GTEx) project. Nat Genet. 2013 Jun;45(6):580-5. doi: 10.1038/ng.2653. PMID: 23715323; PMCID: PMC4010069.

[22] Chen, R.J., Ding, T., Lu, M.Y. et al. Towards a general-purpose foundation model for computational pathology. Nat Med 30, 850–862 (2024). https://doi.org/10.1038/s41591-024-02857-3

[23] Davis, S. R., Pinkerton, J., Santoro, N., & Simoncini, T. (2023). Menopause—Biology, consequences, supportive care, and therapeutic options. Cell, 186(19), 4038–4058. https://doi.org/10.1016/j.cell.2023.08.016

[24] Rosen, Mitchell P., Barbara Sternfeld, Sonya M. Schuh-Huerta, Renee A. Reijo Pera, Charles E. McCulloch, and Marcelle I. Cedars. 2010. “Antral Follicle Count: Absence of Significant Midlife Decline.” Fertility and Sterility 94 (6): 2182–85. https://doi.org/10.1016/j.fertnstert.2009.12.045

[25] Huang Z, Bianchi F, Yuksekgonul M, Montine TJ, Zou J. A visual-language foundation model for pathology image analysis using medical Twitter. Nat Med. 2023 Sep;29(9):2307-2316. doi: 10.1038/s41591-023-02504-3. Epub 2023 Aug 17. PMID: 37592105.

[26] Zhang CP, Yang JL, Zhang J, Li L, Huang L, Ji SY, Hu ZY, Gao F, Liu YX. Notch signaling is involved in ovarian follicle development by regulating granulosa cell proliferation. Endocrinology. 2011 Jun;152(6):2437-47. doi: 10.1210/en.2010-1182. Epub 2011 Mar 22. PMID: 21427220.

[27] Rexxi D Prasasya, Kelly E Mayo, Notch Signaling Regulates Differentiation and Steroidogenesis in Female Mouse Ovarian Granulosa Cells, Endocrinology, Volume 159, Issue 1, January 2018, Pages 184–198, https://doi.org/10.1210/en.2017-00677

[28] Andric N, Ascoli M. The luteinizing hormone receptor-activated extracellularly regulated kinase-1/2 cascade stimulates epiregulin release from granulosa cells. Endocrinology. 2008 Nov;149(11):5549-56. doi: 10.1210/en.2008-0618. Epub 2008 Jul 24. PMID: 18653716; PMCID: PMC2584583.

[29] Baddela VS, Michaelis M, Tao X, Koczan D, Vanselow J. ERK1/2-SOX9/FOXL2 axis regulates ovarian steroidogenesis and favors the follicular-luteal transition. Life Sci Alliance. 2023 Aug 2;6(10):e202302100. doi: 10.26508/lsa.202302100. PMID: 37532283; PMCID: PMC10397509.

[30] Oktay K, Turan V, Titus S, Stobezki R, Liu L. BRCA Mutations, DNA Repair Deficiency, and Ovarian Aging. Biol Reprod. 2015 Sep;93(3):67. doi: 10.1095/biolreprod.115.132290. Epub 2015 Jul 29. PMID: 26224004; PMCID: PMC4710189.

[31] Mills M, Emori C, Kumar P, Boucher Z, George J, Bolcun-Filas E. Single-cell and bulk transcriptional profiling of mouse ovaries reveals novel genes and pathways associated with DNA damage response in oocytes. bioRxiv [Preprint]. 2024 Feb 4:2024.02.02.578648. doi: 10.1101/2024.02.02.578648. Update in: Dev Biol. 2025 Jan;517:55-72. doi: 10.1016/j.ydbio.2024.09.007. PMID: 38352597; PMCID: PMC10862846.

[32] Leem, J., Lee, C., Choi, D.Y. et al. Distinct characteristics of the DNA damage response in mammalian oocytes. Exp Mol Med 56, 319–328 (2024). https://doi.org/10.1038/s12276-024-01178-2

[33] Titus, S., Li, F., Stobezki, R., Akula, K., Unsal, E., Jeong, K., ... & Oktay, K. (2013). Impairment of BRCA1-related DNA double-strand break repair leads to ovarian aging in mice and humans. Science translational medicine, 5(172), 172ra21-172ra21.

[34] Zhang D, Zhang X, Zeng M, Yuan J, Liu M, Yin Y, Wu X, Keefe DL, Liu L. Increased DNA damage and repair deficiency in granulosa cells are associated with ovarian aging in rhesus monkey. J Assist Reprod Genet. 2015 Jul;32(7):1069-78. doi:10.1007/s10815-015-0483-5. Epub 2015 May 10. PMID: 25957622; PMCID: PMC4531862.

[35] Li L, Shi X, Shi Y, Wang Z. The Signaling Pathways Involved in Ovarian Follicle Development. Front Physiol. 2021 Sep 20;12:730196. doi: 10.3389/fphys.2021.730196. PMID: 34646156; PMCID: PMC8504451.

[36] Tepekoy F, Akkoyunlu G. The interaction of Wnt signaling members with growth factors in cultured granulosa cells. Anim Reprod. 2020 Jun 17;17(2):e20190106. doi: 10.1590/1984-3143-AR2019-0106. PMID: 32714449; PMCID: PMC7375871.

[37] Jamnongjit M, Gill A, Hammes SR. Epidermal growth factor receptor signaling is required for normal ovarian steroidogenesis and oocyte maturation. Proc Natl Acad Sci U S A. 2005 Nov 8;102(45):16257-62. doi: 10.1073/pnas.0508521102. Epub 2005 Oct 31. PMID: 16260720; PMCID: PMC1283479.

[38] Ding Y, Zuo Y, Zhang B, Fan Y, Xu G, Cheng Z, Ma S, Fang S, Tian A, Gao D, Xu X, Wang Q, Jing Y, Jiang M, Xiong M, Li J, Han Z, Sun S, Wang S, He F, Yang J, Qu J, Zhang W, Liu GH. Comprehensive human proteome profiles across a 50-year lifespan reveal aging trajectories and signatures. Cell. 2025 Jul 22:S0092-8674(25)00749-4. doi: 10.1016/j.cell.2025.06.047. Epub ahead of print. PMID: 40713952.

[39] Hebbar S, Chaya V, Rai L, Ramachandran A. Factors influencing endometrial thickness in postmenopausal women. Ann Med Health Sci Res. 2014 Jul;4(4):608-14. doi: 10.4103/2141-9248.139340. PMID: 25221714; PMCID: PMC4160690.

[40] Punzon-Jimenez P, Machado-Lopez A, Perez-Moraga R, Llera-Oyola J, Grases D, Galvez-Viedma M, Sibai M, Satorres-Perez E, Lopez-Agullo S, Badenes R, Ferrer-Gomez C, Porta-Pardo E, Roson B, Simon C, Mas A. Effect of aging on the human myometrium at single-cell resolution. Nat Commun. 2024 Jan 31;15(1):945. doi: 10.1038/s41467-024-45143-z. PMID: 38296945; PMCID: PMC10830479.

[41] Zhou, S., Zhao, L., Yi, T. et al. Menopause-induced uterine epithelium atrophy results from arachidonic acid/prostaglandin E2 axis inhibition-mediated autophagic cell death. Sci Rep 6, 31408 (2016). https://doi.org/10.1038/srep31408

[42] Xu S, Yin M, Koroleva M, Mastrangelo MA, Zhang W, Bai P, Little PJ, Jin ZG. SIRT6 protects against endothelial dysfunction and atherosclerosis in mice. Aging (Albany NY). 2016 May;8(5):1064-82. doi: 10.18632/aging.100975. PMID: 27249230; PMCID: PMC4931854.